JOURNAL OF SYNCHROTRON RADIATION
ISSN 1600-5775

Radiochromic film dosimetry in synchrotron radiation breast computed tomography: a phantom study

Giovanni Mettivier,[a,b] Marica Masi,[a,b] Fulvia Arfelli,[c,d]* Luca Brombal,[c,d] Pasquale Delogu,[e,f] Francesca Di Lillo,[a,b,g] Sandro Donato,[c,d] Christian Fedon,[h,d] Bruno Golosio,[i,j] Piernicola Oliva,[k,j] Luigi Rigon,[c,d] Antonio Sarno,[b] Angelo Taibi[l,m] and Paolo Russo[a,b]

[a]Dipartimento di Fisica 'Ettore Pancini', Università di Napoli 'Federico II', I-80126 Napoli, Italy, [b]INFN, Sezione di Napoli, I-80126 Napoli, Italy, [c]Department of Physics, Università di Trieste, I-34127 Trieste, Italy, [d]Sezione di Trieste, INFN, I-34127 Trieste, Italy, [e]Department of Physical Science, Earth and Environment, Università di Siena, I-53100 Siena, Italy, [f]Sezione di Pisa, INFN, I-34127 Pisa, Italy, [g]ELETTRA-Sincrotrone Trieste SCpA, Bassovizza, I-34149 Trieste, Italy, [h]Department of Radiology and Nuclear Medicine, Radboud University Medical Center, 6500 HB Nijmegen, The Netherlands, [i]Department of Physics, Università di Cagliari, I-09042 Cagliari, Italy, [j]Sezione di Cagliari, INFN, I-09042 Cagliari, Italy, [k]Department of Chemistry and Pharmacy, Università di Sassari, Sassari, Italy, [l]Department of Physics and Earth Science, Università di Ferrara, I-44122 Ferrara, Italy, and [m]Sezione di Ferrara, INFN, I-44122 Ferrara, Italy.
*Correspondence e-mail: arfelli@ts.infn.it

Received 30 July 2019
Accepted 7 February 2020

Edited by A. Stevenson, Australian Synchrotron, Australia

Keywords: breast computed tomography; synchrotron radiation; radiochromic dosimetry.

This study relates to the INFN project SYRMA-3D for *in vivo* phase-contrast breast computed tomography using the SYRMEP synchrotron radiation beamline at the ELETTRA facility in Trieste, Italy. This peculiar imaging technique uses a novel dosimetric approach with respect to the standard clinical procedure. In this study, optimization of the acquisition procedure was evaluated in terms of dose delivered to the breast. An offline dose monitoring method was also investigated using radiochromic film dosimetry. Various irradiation geometries have been investigated for scanning the prone patient's pendant breast, simulated by a 14 cm-diameter polymethylmethacrylate cylindrical phantom containing pieces of calibrated radiochromic film type XR-QA2. Films were inserted mid-plane in the phantom, as well as wrapped around its external surface, and irradiated at 38 keV, with an air kerma value that would produce an estimated mean glandular dose of 5 mGy for a 14 cm-diameter 50% glandular breast. Axial scans were performed over a full rotation or over 180°. The results point out that a scheme adopting a stepped rotation irradiation represents the best geometry to optimize the dose distribution to the breast. The feasibility of using a piece of calibrated radiochromic film wrapped around a suitable holder around the breast to monitor the scan dose offline is demonstrated.

1. Introduction

Breast cancer is one of the most frequently diagnosed cancers and one of the leading causes of death for women worldwide (IARC, 2018; ACS, 2019). Early detection is a key factor in treating and defeating this disease (MLN, 2017), and X-ray breast imaging techniques play a fundamental role in this diagnostic task. X-ray imaging of the breast is one of the most challenging imaging modalities, because of the very low contrast of tumor tissue with respect to the surrounding glandular tissue (Chen *et al.*, 2010), and of the high spatial resolution required to detect microcalcifications (down to 0.05−0.1 mm) which could be associated with malignant lesions. Due to its image quality performance combined with low imaging dose, (digital) mammography is essentially the only widely used imaging modality for breast cancer screening

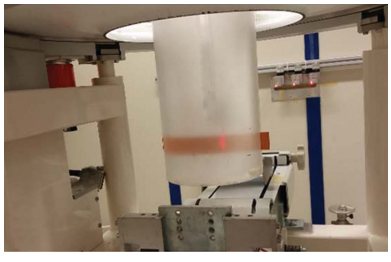

(Karellas & Vedantham, 2008). Digital mammography has intrinsic limitations, being a 2D modality for imaging the complex 3D anatomy of the breast: the superposition of glandular and tumor tissues may hide or mask signs of malignancies, in particular for dense breasts. For these reasons, in addition to digital breast tomosynthesis — which entered the clinical routine very recently as a quasi-tomographic technique for imaging the compressed breast (Sechopoulos, 2013; Maldera *et al.*, 2017) — new 3D imaging modalities for the breast are under investigation, in particular breast computed tomography (CT) with dedicated setups (Sarno *et al.*, 2015; Karellas *et al.*, 2008; Mettivier *et al.*, 2011*a*,*b*). Dedicated breast CT can produce volumetric reconstruction of the uncompressed breast with isotropic resolution. Breast CT maps can also be used for image-guided breast cancer radiotherapy with synchrotron radiation (Di Lillo *et al.*, 2017) or with X-ray tubes (Buonanno *et al.*, 2019). A few research groups have been developing dedicated breast CT prototypes using cone beam geometry (Boone *et al.*, 2001; Gazi *et al.*, 2015; Russo *et al.*, 2010*a*,*b*,*c*; Mettivier *et al.*, 2010, 2011*a*,*b*, 2012*a*,*b*; Kalender *et al.*, 2017; Sarno *et al.*, 2016*b*) and started clinical trials (Lindfors *et al.*, 2008; O'Connell *et al.*, 2010, 2014; Vedantham *et al.*, 2012, 2013). A specific approach uses phase-contrast techniques with the goal of obtaining a better visibility of lesions in breast mammography (Olivo *et al.*, 2013; Scherer *et al.*, 2015; Diemoz *et al.*, 2016; Ando *et al.*, 2016; Castriconi *et al.*, 2016; Arboleda *et al.*, 2017; Ghani *et al.*, 2017) and breast CT (Sarno *et al.*, 2016*b*).

The SYRMA-3D collaboration was established to set up the first clinical trial of phase-contrast breast CT with synchrotron radiation (SR) at the Elettra synchrotron light source facility in Trieste, Italy, based on the previous clinical trial for SR mammography using phase-contrast techniques; that study highlighted an increase of image quality with respect to standard digital mammography (Castelli *et al.*, 2011; Fedon *et al.*, 2018; Longo *et al.*, 2014). Breast imaging with SR may also be compatible with *K*-edge subtraction imaging with iodine contrast medium (Thomlinson *et al.*, 2018) for enhanced visibility of tumor masses. Phase-contrast breast CT with SR employs a parallel, coherent, monoenergetic beam of X-ray photons with the patient in a prone position on a rotating and vertically translating patient support (Longo *et al.*, 2016, 2019; Brombal *et al.*, 2019; Sarno *et al.*, 2016*a*, 2017*a*; Delogu *et al.*, 2017; Taba *et al.*, 2018). Optimal conditions for propagation-based phase-contrast imaging are obtained by using a large source–object distance and by positioning the (photon counting) imaging detector at a distance up to several metres from the vertical axis of rotation (Brombal *et al.*, 2018), where the breast is pendant from an aperture in the patient support. In order to avoid the movement of the breast during the CT procedure the collaboration is studying the possibility of adopting a breast holder or to follow the movement of the breast optically using markers placed on the skin.

Since the maximum vertical height of the SR beam at Elettra is limited to a few millimetres, a partial breast coverage of a few centimetres is feasible during a scan, with a limited number of rotations of the patient support, in a breast CT scan duration of just a few minutes. In order to optimize the irradiation parameters, various axial irradiation geometries are under investigation, with 180° or 360° rotations of the patient support. In this framework, an important parameter is the radiation dose to the glandular tissue in the breast. The main investigative goal of this work was to define which geometry for the CT examination offers appropriate performance in terms of dose distribution in the breast, at a fixed mean glandular dose (MGD) value. In particular, we investigated which irradiation geometry allows a peak of dose deposition (higher than the MGD) to be avoided due to the overlap of more beams in the patient rotate/translate irradiation scheme. This study was conducted on a polymethyl methacrylate (PMMA) cylindrical phantom with dosimetric films inserted into it. In order to assess the surface (skin) dose, and with the additional goal of testing an offline dose monitoring method, we also performed irradiations of radiochromic films wrapped around the phantom, which provided a 2D record of the irradiation history during the whole scan.

It is not obvious which irradiation geometry should be preferred for a breast CT scan with an SR beam, which requires multiple rotations around the pendant breast and a careful selection of the scan pitch: these aspects received little attention in the related literature. Hence, this work aims at understanding the implication of the various possible choices for the irradiation geometry on the 3D dose distribution in the organ. At the same time, this work suggests the use of a permanent record of the irradiation X-ray field incident on the breast during full scan, in the form of a dosimetric film suitably wrapped around the pendant breast: this points towards the need for the definition of quality assurance protocols for SR breast CT, an aspect still unexplored in the literature.

2. Materials and methods

The tomographic setup of the SYRMA-3D project is hosted at the SYRMEP beamline at the Elettra SR facility (Longo *et al.*, 2016, 2019). The patient lies in a prone position, with one of her uncompressed pendant breasts inserted into a circular opening of the patient support, which can fully rotate around a vertical axis and translate in the vertical direction, using a dedicated control system. A PMMA cylindrical phantom of 14 cm in diameter (20 cm height) reproduced an average-size pendant breast. At 38 keV, the photon energy used in the following tests, the PMMA X-ray attenuation (attenuation coefficient $\mu = 0.2898\ \mathrm{cm}^{-1}$) differs by less than 2% from that of breast tissue (ICRU 44) ($\mu = 0.2956\ \mathrm{cm}^{-1}$), while corresponding energy absorption coefficients (μ_{en}) differ by no more than 10%. Values of air kerma measured free-in-air were expressed also after conversion to kerma in PMMA in the phantom (Tomic *et al.*, 2010; Sarno *et al.*, 2017*b*) by the known ratio of mass energy absorption coefficients $(\mu_{\mathrm{en}}/\rho)_{\mathrm{PMMA}}/(\mu_{\mathrm{en}}/\rho)_{\mathrm{air}} = 0.052/0.078 = 0.666$ evaluated at 38 keV (ICRU 44). The phantom was positioned at the isocenter, hanging from the patient support. Measurements were performed at 38 keV photon energy, with a beam size of 3 mm × 150 mm (H × W) defined by a Densimet (tungsten

alloy) slit system, at an air kerma which we estimated to determine an MGD of 5 mGy in a 14 cm-diameter 50% glandular breast. This estimated MGD was kept constant for all irradiation conditions, by suitably changing the incident air kerma, following the methods of Mettivier *et al.* (2016).

2.1. Experimental setup

The SYRMEP beamline dosimetry system consists of two high-precision custom ionization chambers (IOC1 and IOC2), designed and constructed at the Elettra laboratories specifically for the laminar beam geometry. The IOCs response was calibrated against the air kerma primary standard of the INMRI-ENEA (Italian National Institute for the Ionizing Radiation Metrology) (Bovi *et al.*, 2007). From the ionization chamber reading, through proper conversion factors, the air kerma is calculated at the phantom position. The ionization chamber used for this work is the first one, IOC1, which is placed upstream of the shutters, in order to measure the dose rate irradiating the phantom. For air kerma measurement inside the phantom, we used another ionization chamber, type Semiflex 31010 (PTW Freiburg, Germany), with air kerma values read using a PTW Unidos E dosimeter. The IOC1 chamber and the Semiflex ionization chamber were intercalibrated by exposure to a uniform X-ray field with photon energy of 38 keV (Prezado *et al.*, 2011). We paid attention to irradiate the whole and only sensitive volume of the Semiflex ionization chamber in order to reduce the air scatter (Bovi *et al.*, 2007). To simulate a breast CT scan, the cylindrical PMMA phantom was positioned at the center of rotation of the scanner, hanging from the patient support [Figs. 1(*a*) and 1(*b*)]. The phantom approximates the cylindrical symmetry and the mean diameter of the breast at the chest wall (Boone *et al.*, 2004); it was made of two half-cylinders held together by nylon bolts (so that a film piece can be inserted at mid-plane), with a central cavity for hosting an ionization chamber. The radiochromic films were cut into two long rectangular strips and wrapped tightly around the phantom, in order to measure the entrance surface air kerma ('skin dose') [Fig. 1(*b*)], in addition to the air kerma measured at mid-plane ('internal dose') by the films, calibrated in terms of air kerma [Fig. 1(*a*)]. The radiochromic films used were of the type GafChromic™ XR-QA2 (sheet size 25.40 cm × 30.48 cm, lot No. 01041701; Ashland Inc., USA). Two strips cut out of a film sheet covered the entire circumference of the PMMA phantom without overlap. The height of the film strips was varied and was chosen to comfortably contain the vertical profile of the beam. This configuration is shown in Figs. 1(*a*) and 1(*b*).

2.2. Irradiation geometry/modality

In each irradiation test, the strips of radiochromic films were exposed to an incident air kerma at the isocenter which we calculated to deliver, for a breast with 50% glandular fraction, a fixed MGD of 5 mGy for the volume irradiated by the SR beam. In order to calculate the correct MGD value in our peculiar irradiation geometry, where the breast is not completely irradiated, we have developed a dedicated

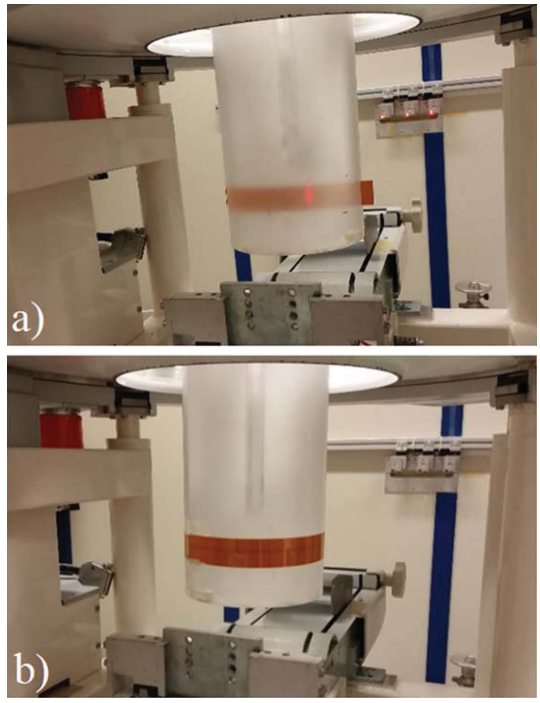

Figure 1
The PMMA cylindrical phantom pendant from the hole in the patient support; in the background the rectangular beam entrance window can be seen. (*a*) A flat piece of radiochromic film is positioned in the middle of the phantom to record the 2D distribution of the incident air kerma. (*b*) A radiochromic film strip is wrapped around the phantom using adhesive tape; its central part shows a thin blackened rectangular area where the SR beam is incident on the phantom.

GEANT4 simulation code (Mettivier *et al.*, 2016). We adopted three irradiation geometries (Fig. 2), indicated below, in order to simulate different modalities of breast CT scans that are under study for the implementation of the clinical examination:

(i) *Full single-scan modality*. The radiochromic film was irradiated only once while the patient support made a 360° rotation with an angular speed of 12.4° s^{-1}, for a total irradiation time of 29 s [Fig. 2(*a*)].

(ii) *Half step-scan modality*. The radiochromic film was irradiated while the patient support rotated through an arc of 180° [Fig. 2(*b*)]. Then, the beam was switched off and the patient support was moved in the vertical direction by a distance of 3.00 mm (equal to the beam height at the slits position). The patient support was moved back to the 0° position and the irradiation was repeated with the same 0−180° angular span as in the first rotation. The patient support was moved to three different vertical positions. The patient support angular speed during each rotation was 6.21° s^{-1}, so that each slice of the phantom was exposed for 29 s. The total exposure time was 87 s.

(iii) *Full step-scan modality*. The film was irradiated once while the patient support made a rotation in the arc 0−180°, then the beam was switched off and the patient support was moved in the vertical direction by a 3 mm step (equal to the beam height at the slits position). The film was then irradiated while the patient support made another 180° rotation in the

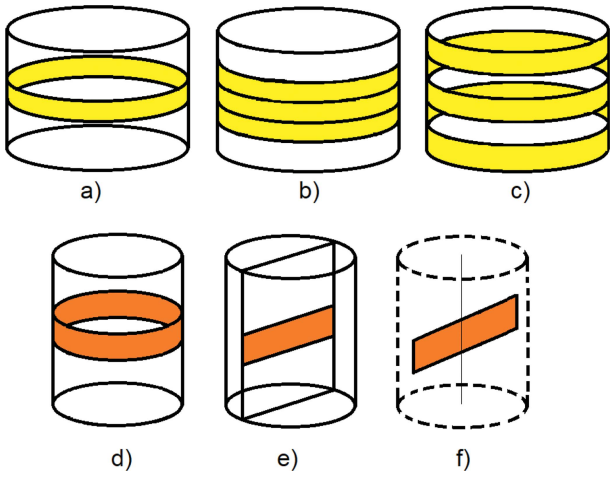

Figure 2
Irradiation geometries. (*a*) Full single-scan modality; (*b*) half step-scan modality; (*c*) full step-scan modality. The yellow areas indicate the area irradiated by the incident X-ray beam on the surface of the cylindrical phantom. Shown in (*d*), (*e*), (*f*) are the positions of the radiochromic film positioned all around the surface of the cylinder, at the midplane and at the isocentre without the phantom, respectively.

arc 180–360°. This sequence was then repeated starting again from the 0° position. The patient support was moved to six different vertical positions. The patient support angular speed during rotation was 6.21° s^{-1}, exposing each slice for 29 s [Fig. 2(*c*)].

The choice of these geometries is related to their equivalence in terms of imaging results thanks to the parallel propagation geometry of the beam. In this geometry, the acquisition of projections on 180° is completely equivalent to an acquisition on 360° in terms of a complete reconstruction of the object. Even though the image quality (and total dose) is the same, the dose distribution inside the breast should differ. The 360° rotation was chosen in order to obtain a symmetric dose distribution while the other two modalities were chosen in order to reduce the number of rotations that the patient must experience.

2.3. Radiochromic dosimetry protocol

The evaluation of the radiochromic film response (Devic *et al.*, 2016) was performed following the procedure described by Tomic *et al.* (2010, 2014) and Di Lillo *et al.* (2016). Each film was scanned always in the same position at the center of a flatbed document scanner (Epson Perfection 850 Pro, readout by EPSON Scan software). The position of each film on the scanner was fixed by using rectangular paper frames; during the scanning process, to avoid the Newton rings phenomenon, we positioned three frames under the film pieces, so that the films were not in direct contact with the scanner glass surface. Then we covered the white side of the radiochromic film with a white paper in order to block residual transmission through the film. Films were scanned in reflectance mode before exposure, and after about 48 h they were irradiated. The scanning resolution was set to 96 dots per inch (264 µm pixel size). Three 48-bit RGB scans (16-bit per channel) were obtained and saved in TIFF file format. Only the red channel of the RGB image was used to analyze the films, where the film sensitivity is higher. Film pieces were scanned one at a time, four times in total, but only the last three scans were used for evaluation. For each scan we measured the pixel value (PV) using the freeware image analysis program *ImageJ* (Rasband, 2018). The reflectance change (ΔR) after irradiation was evaluated as follows,

$$\Delta R = R_{\rm Before} - R_{\rm After} = \frac{{\rm PV}_{\rm Before}}{2^{16}} - \frac{{\rm PV}_{\rm After}}{2^{16}}, \qquad (1)$$

where 2^{16} is the maximum observable value in a 16-bit depth image. By error propagation, the corresponding uncertainty $\sigma_{\Delta R}$ was calculated as

$$\sigma_{\Delta R} = \frac{1}{2^{16}}\left(\sigma^2_{{\rm PV}_{\rm Before}} + \sigma^2_{{\rm PV}_{\rm After}}\right)^{1/2}. \qquad (2)$$

A control film piece was kept unirradiated to quantify the variation in net reflectance due to other effects, such as scanning light, natural light, temperature, humidity, *etc.* (Aldelaijan *et al.*, 2016). We handled this control film piece in the same way as the other scanned pieces, and we scanned it before as well as after the irradiations. The difference in the measured reflectance in the control film piece was obtained as

$$\Delta R^{\rm Control} = R^{\rm Control}_{\rm Before} - R^{\rm Control}_{\rm After} = \frac{{\rm PV}^{\rm Control}_{\rm Before}}{2^{16}} - \frac{{\rm PV}^{\rm Control}_{\rm After}}{2^{16}}. \qquad (3)$$

The net reflectance change due to irradiation was obtained by subtracting the net reflectance change in the irradiated and the control film pieces,

$$\text{net}\,\Delta R = \Delta R - \Delta R^{\rm Control}, \qquad (4)$$

with an uncertainty $\sigma_{\text{net}\,\Delta R}$,

$$\sigma_{\text{net}\,\Delta R} = \left[(\sigma_{\Delta R})^2 + \left(\sigma^{\rm Control}_{\Delta R}\right)^2\right]^{1/2}. \qquad (5)$$

XR-QA2 radiochromic films were calibrated in terms of free-in-air air kerma. Several 4 cm × 4 cm films were positioned in a PMMA frame pendant from the hole in the patient support, and they were completely exposed to the X-ray beam at different air kerma values in the range 1–20 mGy moving the beam in the vertical direction. For each film, net ΔR was estimated as explained above. The calibration curve for the photon energy of the beam (in this case 38 keV) was obtained by plotting the air kerma as a function of the corresponding film response net ΔR [Fig. 3(*a*)]. The choice of the power law form of the calibration curve was based on the criteria explained by Tomic *et al.* (2014). The uncertainty analysis relative to the fitting function was made following Devic *et al.* (2004) and is reported in Fig. 3(*b*). As deduced from this figure, for values of air kerma above 5 mGy, the total uncertainty was less than 5%.

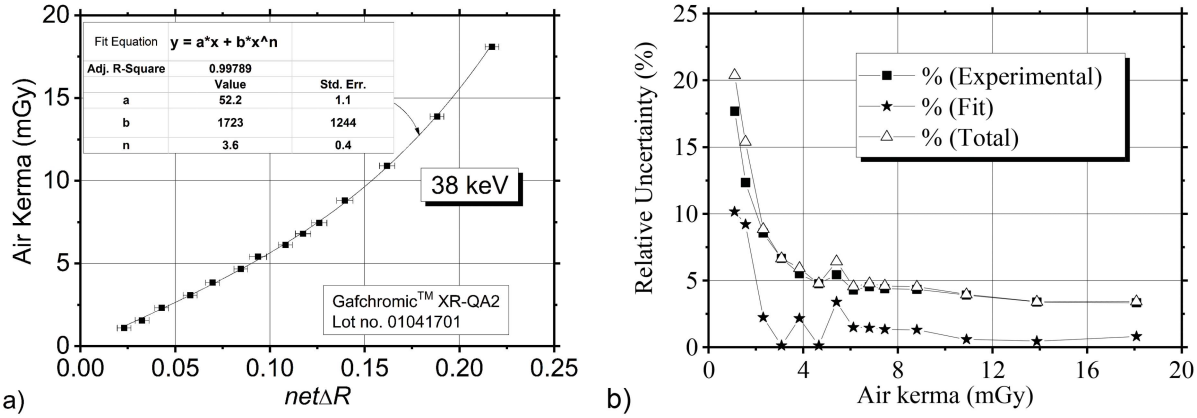

Figure 3
(*a*) Calibration of the XR-QA2 radiochromic film batch at 38 keV. The experimental points have been least-squares-fitted by a power function. (*b*) Total relative dose uncertainty, fitting and experimental uncertainties as a function of air kerma measured free in air.

3. Results

3.1. Beam profile measurement

First of all, we measured the air kerma map produced by the beam in air on the radiochromic film, following Di Lillo *et al.* (2015). The setup is shown in Fig. 4, while Fig. 5 shows the measurement results. The map of the beam air kerma expressed in mGy is reported in Fig. 5(*a*), where the white area indicates the film zone where the SR beam was incident. The vertical and horizontal profiles of this 2D distribution are reported in Figs. 5(*b*) and 5(*c*), respectively. Fig. 5(*b*) shows a bell-shaped vertical distribution of the beam, whose measured FWHM is equal to 3.35 mm. Comparing the FWHM with the beam height at the slits position (3.00 mm), we observed that a 12% beam magnification is present between the vertical size of the beam at the surface of the phantom with respect to the beam vertical size upstream at the position of the collimator slits. The intensity of the beam is quite uniform along the horizontal direction for a total length of 160 mm: the air kerma variations along the horizontal profile have a standard

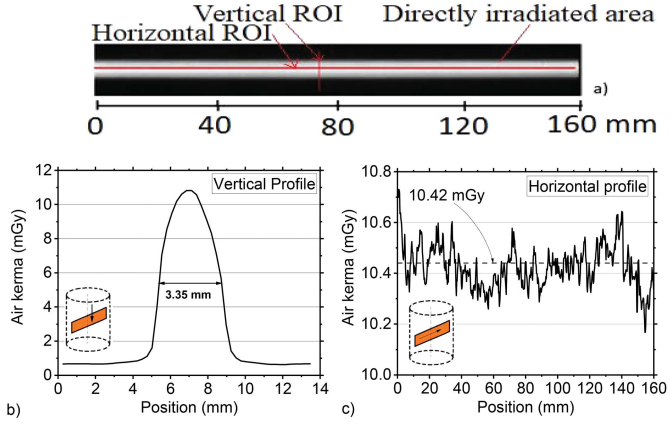

Figure 5
(*a*) Scan of the exposed radiochromic film positioned at the isocenter perpendicular to the incident beam; dose profiles were evaluated along the indicated horizontal and vertical red lines. (*b*) Vertical profile and (*c*) horizontal profile of the beam measured free in air. The inset shows the position of the film. These profiles show a bell-shaped vertical distribution (*b*) of the beam (FWHM = 3.35 mm) and a quite uniform intensity of the beam along the horizontal direction (*c*) with a standard deviation of 0.08 mGy around a mean value of 10.42 mGy.

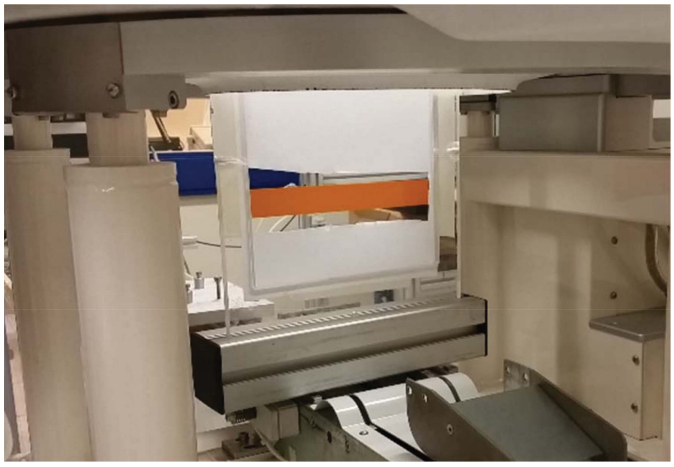

Figure 4
Photograph of the under-table beam profile measurement setup, using a flat piece of radiochromic film positioned at the isocenter, normal to the incident beam.

deviation of only 0.08 mGy around a mean value of 10.42 mGy [Fig. 5(*c*)], well below the 5% uncertainty limit of our film dosimeters.

3.2. Full single-scan modality

3.2.1. Skin dose. Fig. 6(*a*) shows the surface (skin) dose distribution for the 360° irradiation. The dose distribution is almost uniform through the whole length of the film [Fig. 6(*c*)], since all the parts of the film were exposed equally to the X-ray beam during the 360° rotation of the phantom. We performed a quantitative analysis of the dose distribution profiles in Figs. 6(*b*) and 6(*c*). The dose distribution profile, see Fig. 6(*b*), shows the air kerma along the vertical direction measured at 90° in a 2 mm × 10 mm region of interest (ROI). The distribution is bell-shaped with a FWHM of 3.38 mm. Fig. 6(*c*) shows the horizontal profile of dose distribution measured in a 3 mm × 145 mm ROI, with a mean value of

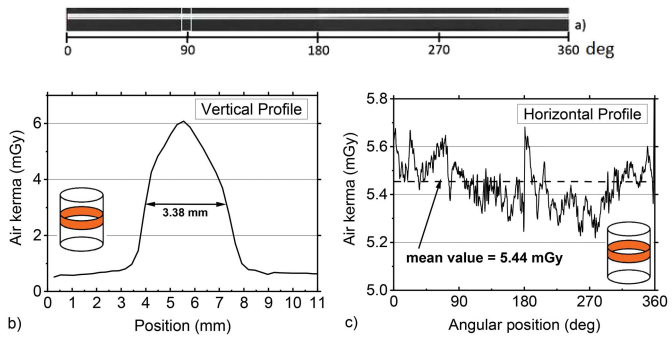

Figure 6
Full single-scan modality to the skin. (*a*) Scan of the exposed radiochromic film; average dose profiles were evaluated in the horizontal and vertical ROIs indicated by the two rectangles in white. (*b*) Vertical profile (with indication of the FWHM) and (*c*) horizontal profile of the dose distribution. The vertical profile is bell-shaped with a FWHM of 3.38 mm while the horizontal profile (*c*) has a mean value of 5.44 mGy and a standard deviation of 1.8% around the mean value. These fluctuations are consistent with the radiochromic film dosimetry uncertainty. The insets show the position of the film on the surface of the cylindrical phantom.

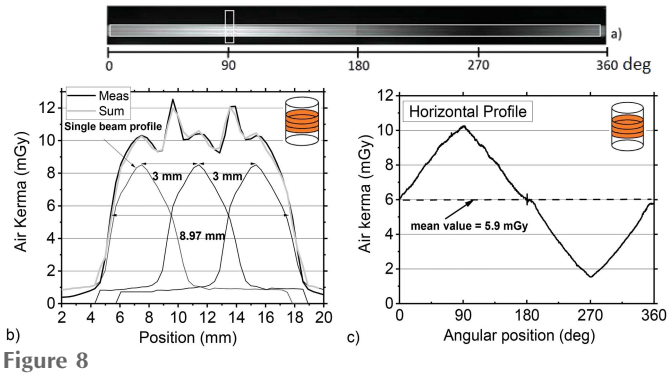

Figure 8
Half step-scan irradiation modality. (*a*) Scan of the exposed radiochromic film; average dose profiles were evaluated in the horizontal and vertical ROIs indicated by the two rectangles in white. (*b*) Vertical profile, and (*c*) horizontal profile of the dose distribution to the skin. In (*b*) the measured dose profile (thick line) is compared with the profile (in light gray) derived from summing the three line profiles each measured from a single scan, after successive 3 mm shifts of the position of the incident beam. The insets show the position of the film on the surface of the cylindrical phantom.

5.44 mGy and a standard deviation of 1.8% around the mean value. These fluctuations are consistent with the radiochromic film dosimetry uncertainty.

3.2.2. Internal dose. Fig. 7 shows a dose (and air kerma) map evaluated at the mid-plane in the phantom, indicating the cup-shaped horizontal profile due to primary and scatter dose. The position of the cylinder walls is indicated in the figure. The scatter contribution can be also quantified in the FWHM value of the vertical profile of 3.56 mm. It is 1.2 times the beam dimension to the slit position and, due to the scatter inside the phantom, 1.05 times the beam dimension at the cylinder entrance.

3.3. Half step-scan modality

3.3.1. Skin dose. The skin dose distributions of the half step-scan modality are shown in Fig. 8. In order to assess the observed superposition of the dose, it is interesting to study

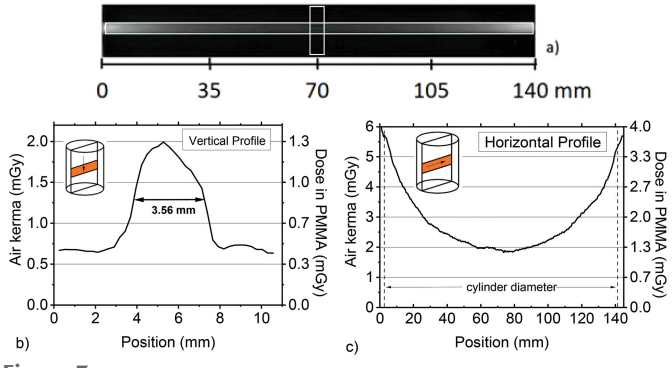

Figure 7
Full single-scan modality at the mid-plane in the phantom. (*a*) Scan of the exposed radiochromic film; average dose (and air kerma) profiles were evaluated in the horizontal and vertical ROIs indicated by the two rectangles in white. (*b*) Vertical profile, and (*c*) horizontal profile of the dose distribution. The insets show the position of the film in the phantom.

the vertical profile of the dose distribution. The plot in Fig. 8(*b*) has been obtained by selecting a vertical ROI at 90°. In particular, Fig. 8(*b*) shows the single beam profiles [Fig. 6(*b*)] shifted by 3 mm and their sum, in addition to the measured vertical beam profile. The overlap between the measured and calculated beam profile is remarkable.

Fig. 8(*c*) shows the horizontal dose distribution. The air kerma increases in the first 90° of the rotation, then it reaches a maximum value, since at 90° this part was exposed directly to the beam during the 180° rotation. Then the air kerma reaches a minimum in the successive 180° and then starts to increase again. Approximately, the point at 0° was directly in front of the beam at the beginning of the irradiation, while the point at 90° was on the edge of the cylindrical phantom and was exposed directly to the beam throughout the rotation. The maximum air kerma variation around the mean value is equal to 75%. The regions that present the lowest dose have never been directly exposed to the beam during the rotation, yet they have received a dose that is at least 13% of the maximum dose. This dose is due both to the radiation scattered by the air and the PMMA phantom and to the transmission of the X-ray beam through the double layer of radiochromic film and the phantom.

3.3.2. Internal dose. The dose (and air kerma) measured in the middle of the phantom is reported in Fig. 9. Also, in this case it is possible to see the same effect due to the beam superposition that we have seen on the skin. The minimum dose value in the horizontal profile is about 3 mGy.

3.4. Full step-scan modality

3.4.1. Skin dose. The surface ('skin') dose distribution of the full step-scan modality is shown in Fig. 10. We can see horizontal stripes in the irradiated area of the film corresponding to the different vertical translations of the patient support. We can observe areas of higher dose both in the first and second half of the film, in agreement with the different

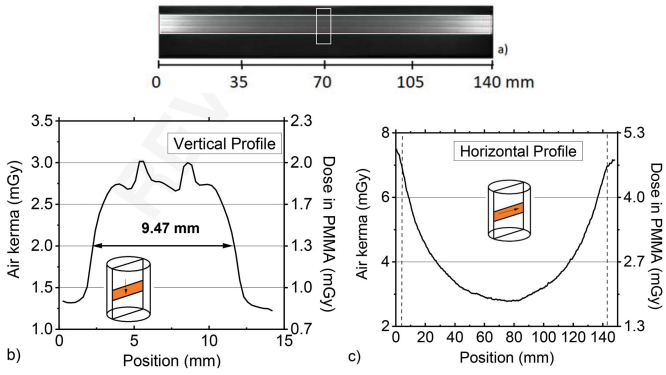

Figure 9
Half step-scan modality at the mid-plane in the phantom. (*a*) Scan of the exposed radiochromic film; average dose (and air kerma) profiles were evaluated in the horizontal and vertical ROIs indicated by the two rectangles in white. (*b*) Vertical profile, and (*c*) horizontal profile of the dose distribution. The insets show the position of the film placed in the phantom.

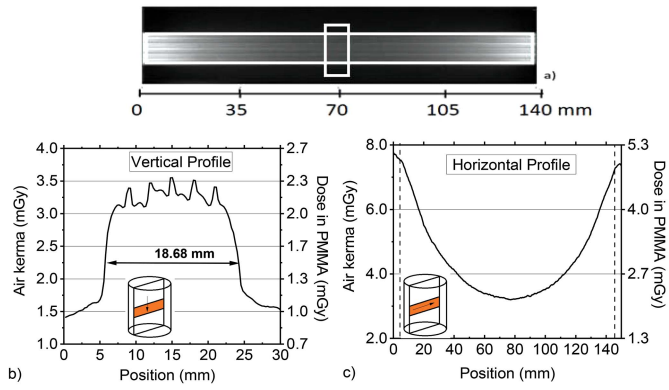

Figure 11
Full step-scan modality at the mid-plane in the phantom. (*a*) Scan of the exposed radiochromic film; average dose (and air kerma) profiles were evaluated in the horizontal and vertical ROIs indicated by the two rectangles in white. (*b*) Vertical profile and (*c*) horizontal profile of the dose distribution. The insets show the position of the film in the phantom.

irradiation scheme. For example, starting from the first slice (odd slice) from the bottom, we can find the previously observed horizontal pattern [Fig. 10(*c*)]: it increases in the first 90° of the film and reaches a maximum value, while at 270° it reaches a minimum and then starts to increase again. Conversely, in the adjacent slice (even slice) the dose reaches the minimum in the first half and the maximum in the second half of the film because in this case the rotation was performed in the arc 180−360°. This pattern is repeated for all the even and odd slices. In both the even and the odd slices a maximum relative dose variation of about 34% is observed.

This irradiation scheme allows to alternate areas of higher and lower dose, hence, differently from the half step-scan modality, only a partial overlap in the valleys of the vertical dose profile can be observed [Fig. 10(*b*)]. The three peaks observed in the figure, corresponding to the even slices, have the same shape, while the maximum peak-to-valley difference is equal to 75% of the maximum dose. Nevertheless, superpositions between consecutive irradiations can be appreciated in the greyscale image in Fig. 10(*a*), in the central region of the film, where intermediate dose values of contiguous slices partially overlap.

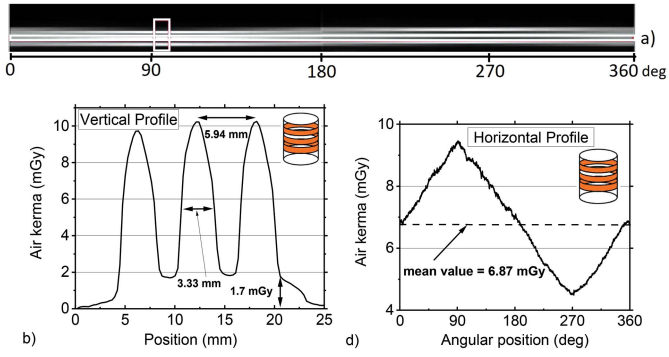

Figure 10
Full step-scan modality to the skin. (*a*) Scan of the exposed radiochromic film; average dose profiles were evaluated in the horizontal and vertical ROIs indicated by the two rectangles in white. (*b*) Vertical profile and (*c*) horizontal profile of the dose distribution. The insets show the position of the film wrapped on the phantom surface.

3.4.2. Internal dose. The plot in Fig. 11(*b*) has been obtained by selecting a vertical ROI in the center of the film [Fig. 11(*a*)]. We can clearly see the peaks given by the superposition of adjacent slices; anyway, the dose maximum value and the horizontal profile [Fig. 11(*c*)] are similar to the one obtained in the half step-scan modality with an air kerma of 3.2 mGy at the phantom center.

4. Discussion

Phase-contrast breast CT with synchrotron radiation is a new imaging procedure under investigation at the Elettra facility with the aim to move towards clinical practice in the near future. At this stage it is fundamental to establish an acquisition protocol based on the peculiar geometry of the beam, on the optimization of the image quality and on the reduction of the dose to patient. In particular, the evaluation of the deposited dose in this examination is linked to the features of the beam (*i.e.* beam geometry, monochromaticity, *etc.*) and does not find correspondence in other diagnostic examinations. The problem of finding the best irradiation geometry in order to optimize the dose deposition is directly related to the use of a synchrotron beam. This is the first study where these aspects were evaluated.

For our project of SR *in vivo* CT dedicated to the breast, we used calibrated XR-QA2 radiochromic films for relative dosimetry in the setup currently under realization at the SYRMEP beamline of the Elettra SR facility. The irradiation setup includes a rotating and vertically translating patient support; the vertical translation allows breast scan, in successive rotations of the support, over a larger vertical range than permitted by the few-millimetre beam height. We observed that the XR-QA2 radiochromic films exposed to free air kerma up to 12 mGy reproduced with fidelity the dose map at the surface and in the bulk of the breast phantom, showing all

subtle changes (down to a fraction of a milligray) in the dose maps produced by the overlapping beam irradiations.

In this phantom study, the comparison of dose maps in different irradiation geometries allowed us to identify the 'suitable' irradiation geometry, in terms of limited spread of the dose distribution during the breast SR CT examination, for a fixed value of the estimated mean glandular dose. Indeed, the 3D dose map in the irradiated object has significant variations, determined by the rotational dose delivery and by the specific irradiation adopted. In particular, local maxima in the dose maps – evaluated on the surface and at the midplane in the irradiated object – arise in regions of overlap between two adjacent irradiated areas, as produced in successive translations/rotations of the support. In the optimized irradiation setup there should be limited zones in the sample where the dose is significantly higher than the average value. We investigated three irradiation geometries by measuring the dose delivery to the external surface (skin) and to the mid-plane of a cylindrical phantom, simulating the pendant breast.

As a metric for skin dose we used the film response calibrated in terms of air kerma free-in-air. In the 180° irradiation (half step-scan), we observed that the non-irradiated areas of the phantom surface received a dose of about 15% of the maximum dose delivered to the exposed skin, due to the scatter radiation and to the radiation transmitted through the phantom. Comparing the horizontal dose distribution for the 180° and the 360° irradiations, we observed that, even if the corresponding estimated MGD is the same, the dose distribution is different since the 360° irradiation (full single-scan, full step-scan) spreads the dose around the circumference in a more homogeneous way than the 180° irradiation (half step-scan). Concerning the half step-scan irradiation, in the vertical profile we noticed areas of superposition with a higher-than-desirable delivered dose to the skin. The full step-scan irradiation appears to be the best choice, since it presents no superposition and a similar dose distribution (the skin-to-center dose ratio is only 2.2). Results of all measurements are collected in Table 1.

Table 1
Dosimetric evaluation in terms of air kerma free-in-air in full single-scan, half step-scan and full step-scan irradiation geometries.

	Revolutions	Internal dose (min) (mGy)	Skin dose (max) (mGy)	Average skin dose (mGy)	Skin-to-center dose ratio
Full single-scan	1	1.9	6	5.4	2.9
Half step-scan	3	2.8	12	5.9	2.1
Full step-scan	6	3.2	10	6.9	2.2

Another interesting aspect that emerged in these tests is the possibility to correlate the average dose measured on the skin (via a radiochromic film piece wrapped around the surface of a PMMA cylindrical tube placed under-table around the breast) with the MGD delivered to the patient during the examination. This gives the possibility, after terminating the examination, of using a radiochromic film piece (wrapped around the breast holder, used to protect and fix the breast during the examination) as an offline dose monitoring tool to control the correct delivery of the dose. This approach may represent a first step towards the introduction of quality assurance protocols for *in vivo* SR breast CT, where the irradiation field can be recorded before the examination, as well as during the examination and then analyzed off-line. Moreover, via suitable Monte Carlo simulation, the dose recorded at the surface of the breast with a strip of radiochromic film can be utilized post-examination to estimate the glandular dose in the breast volume.

We point out that we used a homogeneous PMMA phantom, this being a limitation of this study. Indeed, in general PMMA is not an ideal material for simulating the energy absorption in the breast tissues. However, since our study points to adopting a beam photon energy of 38 keV, PMMA has a corresponding energy absorption coefficient which differs by less than 10% from that of the breast tissue (with composition defined according to ICRU 44). Hence, our cylindrical PMMA object is a reasonable phantom for the pendant breast, though the dose to PMMA is only proportional to the dose to the glandular fraction of the corresponding-size whole breast. Moreover, a homogeneous phantom does not reproduce the breast tissue anatomy of any patient. For a more accurate evaluation of the dose to the glandular fraction of the breast, a realistic breast model would be appropriate. We have recently adopted a new approach in which a real breast anatomy is realized via a 3D printed phantom with three components mimicking the skin, the adipose and the glandular tissue, respectively (Ivanov *et al.*, 2018; Esposito *et al.*, 2019). Such phantoms may incorporate breast tumor models as we investigated recently (Dukov *et al.*, 2019; Bliznakova *et al.*, 2019). Characterization of these new phantoms for absorption-based and phase-contrast-based SR breast CT is ongoing.

5. Conclusions

The evaluation of deposited dose in phase-contrast breast CT with synchrotron radiation is influenced by the features of the beam and in particular by its laminar geometry which implies a scan of the patient through the beam which does not find correspondence in other diagnostic examinations. This calls for a novel dosimetric approach with respect to the standard clinical procedure. For this reason, we performed irradiations of radiochromic films wrapped around, and placed inside, an acrylic cylindrical breast phantom, which provided a 2D record of the irradiation history during the whole scan. For the setup currently under realization at the SYRMEP beamline of the Elettra SR facility, we performed this study in order to evaluate which geometry for the SR CT examination offers appropriate performance in terms of more homogeneous dose distribution in the breast. From this work we derived an indication that the best irradiation geometry is the full step-scan modality. This modality allows a homogeneous skin dose distribution to be obtained without the undesired partial

overlaps of the beam profile at different vertical steps during the acquisition. As an additional result, we have demonstrated the feasibility of using a radiochromic film wrapped around the breast holder as an offline dose monitoring method to have an indirect indication of the delivered dose during the examination.

Funding information

This research has been supported by Istituto Nazionale di Fisica Nucleare (INFN, project SYRMA-3D).

References

ACS (2019). *American Cancer Society: Breast Cancer*, https://www.cancer.org/cancer/breast-cancer.html. Accessed online on 03/01/2019.

Aldelaijan, S., Alzorkany, E., Moftah, B., Buzurovic, I., Seuntjens, J., Tomic, N. & Devic, S. (2016). *Phys. Med.* **32**, 202–207.

Ando, M., Sunaguchi, N., Shimao, D., Pan, A., Yuasa, T., Mori, K., Suzuki, Y., Jin, G., Kim, J. K., Lim, J. H., Seo, S. J., Ichihara, S., Ohura, N. & Gupta, R. (2016). *Phys. Med.* **32**, 1801–1812.

Arboleda, C., Wang, Z., Koehler, T., Martens, G., Van Stevendaal, U., Bartels, M., Villanueva-Perez, P., Roessl, E. & Stampanoni, M. (2017). *Opt. Express*, **25**, 6349–6364.

Bliznakova, K., Dukov, N., Feradov, F., Gospodinova, G., Bliznakov, Z., Russo, P., Mettivier, G., Bosmans, H., Cockmartin, L., Sarno, A., Kostova-Lefterova, D., Encheva, E., Tsapaki, V., Bulyashki, D. & Buliev, I. (2019). *Phys. Med.* **64**, 293–303.

Boone, J. M., Nelson, T. R., Lindfors, K. K. & Seibert, J. A. (2001). *Radiology*, **221**, 657–667.

Boone, J. M., Shah, N. & Nelson, T. R. (2004). *Med. Phys.* **31**, 226–235.

Bovi, M., Laitano, R. F., Pimpinella, M., Quai, E., Tromba, G., Vascotto, A. & Dreossi, D. (2007). *Workshop on Absorbed Dose and Air Kerma Primary Standards*, 9–11 May, 2007, Paris, France.

Brombal, L., Donato, S., Dreossi, D., Arfelli, F., Bonazza, D., Contillo, A., Delogu, P., Di Trapani, V., Golosio, B., Mettivier, G., Oliva, P., Rigon, L., Taibi, A. & Longo, R. (2018). *Phys. Med. Biol.* **63**, 24NT03.

Brombal, L., Golosio, B., Arfelli, F., Bonazza, D., Contillo, A., Delogu, P., Donato, S., Mettivier, G., Oliva, P., Rigon, L. & Taibi, A. (2019). *J. Med. Imag.* **6**, 031402.

Buonanno, F., Sarno, A., De Lucia, P. A., Di Lillo, F., Masi, F., Di Franco, F., Mettivier, G. & Russo, P. (2019). *Phys. Med.* **62**, 63–72.

Castelli, E., Tonutti, M., Arfelli, F., Longo, R., Quaia, E., Rigon, L., Sanabor, D., Zanconati, F., Dreossi, D., Abrami, A., Quai, E., Bregant, P., Casarin, K., Chenda, V., Menk, R. H., Rokvic, T., Vascotto, A., Tromba, G. & Cova, M. A. (2011). *Radiology*, **259**, 684–694.

Castriconi, R., Mettivier, G. & Russo, P. (2016). *Proceedings of the 13th International Workshop on Breast Imaging (IWDM 2016)*, Vol. 9699 of *Lecture Notes in Computer Science*, edited by A. Tingberg, K. Lång and P. Timberg. Berlin, Heidelberg: Springer.

Chen, R. C., Longo, R., Rigon, L., Zanconati, F., De Pellegrin, A., Arfelli, F., Dreossi, D., Menk, R. H., Vallazza, E., Xiao, T. Q. & Castelli, E. (2010). *Phys. Med. Biol.* **55**, 4993–5005.

Delogu, P., Golosio, B., Fedon, C., Arfelli, F., Bellazzini, R., Brez, A., Brun, F., Lillo, F. D., Dreossi, D., Mettivier, G., Minuti, M., Oliva, P., Pichera, M., Rigon, L., Russo, P., Sarno, A., Spandre, G., Tromba, G. & Longo, R. (2017). *J. Instrum.* **12**, C01016.

Devic, S., Seuntjens, J., Hegyi, G., Podgorsak, E. B., Soares, C. G., Kirov, A. S., Ali, I., Williamson, J. F. & Elizondo, A. (2004). *Med. Phys.* **31**, 2392–2401.

Devic, S., Tomic, N. & Lewis, D. (2016). *Phys. Med.* **32**, 541–556.

Diemoz, P. C., Bravin, A., Sztrókay-Gaul, A., Ruat, M., Grandl, S., Mayr, D., Auweter, S., Mittone, A., Brun, E., Ponchut, C., Reiser, M. F., Coan, P. & Olivo, A. (2016). *Phys. Med. Biol.* **61**, 8750–8761.

Di Lillo, F., Mettivier, G., Sarno, A., Castriconi, R. & Russo, P. (2017). *Phys. Med.* **41**, 20–25.

Di Lillo, F., Mettivier, G., Sarno, A., Tromba, G., Tomic, N., Devic, S. & Russo, P. (2016). *Med. Phys.* **43**, 583–588.

Dukov, N., Bliznakova, K., Feradov, F., Buliev, I., Bosmans, H., Mettivier, G., Russo, P., Cockmartin, L. & Bliznakov, Z. (2019). *Phys. Med.* **57**, 80–87.

Esposito, G., Mettivier, G., Bliznakova, K., Bliznakov, Z., Bosmans, H., Bravin, A., Buliev, I., Di Lillo, F., Ivanov, D., Minutillo, M., Sarno, A., Vignero, J. & Russo, P. (2019). *Phys. Med. Biol.* **64**, 075008.

Fedon, C., Rigon, L., Arfelli, F., Dreossi, D., Quai, E., Tonutti, M., Tromba, G., Cova, M. A. & Longo, R. (2018). *J. Med. Imaging*, **5**, 013503.

Gazi, P. M., Yang, K., Burkett, G. W., Aminololama-Shakeri, S., Anthony Seibert, J. & Boone, J. M. (2015). *Med. Phys.* **42**, 1973–1981.

Ghani, M. U., Wong, M. D., Wu, D., Zheng, B., Fajardo, L. L., Yan, A., Fuh, J., Wu, X. & Liu, H. (2017). *Phys. Med. Biol.* **62**, 3523–3538.

IARC (2018). *Global cancer facts sheets: Breast cancer*, http://gco.iarc.fr/today/data/factsheets/cancers/20-Breast-fact-sheet.pdf.

Ivanov, D., Bliznakova, K., Buliev, I., Popov, P., Mettivier, G., Russo, P., Di Lillo, F., Sarno, A., Vignero, J., Bosmans, H., Bravin, A. & Bliznakov, Z. (2018). *Phys. Med. Biol.* **63**, 175020.

Kalender, W. A., Kolditz, D., Steiding, C., Ruth, V., Lück, F., Rößler, A. C. & Wenkel, E. (2017). *Eur. Radiol.* **27**, 1081–1086.

Karellas, A., Lo, J. Y. & Orton, C. G. (2008). *Med. Phys.* **35**, 409–411.

Karellas, A. & Vedantham, S. (2008). *Med. Phys.* **35**, 4878–4897.

Lillo, F. D., Dreossi, D., Emiro, F., Fedon, C., Longo, R., Mettivier, G., Rigon, L., Russo, P. & Tromba, G. (2015). *J. Instrum.* **10**, C05002.

Lindfors, K. K., Boone, J. M., Nelson, T. R., Yang, K., Kwan, A. L. C. & Miller, D. F. (2008). *Radiology*, **246**, 725–733.

Longo, R., Arfelli, F., Bellazzini, R., Bottigli, U., Brez, A., Brun, F., Brunetti, A., Delogu, P., Di Lillo, F., Dreossi, D., Fanti, V., Fedon, C., Golosio, B., Lanconelli, N., Mettivier, G., Minuti, M., Oliva, P., Pinchera, M., Rigon, L., Russo, P., Sarno, A., Spandre, G., Tromba, G. & Zanconati, F. (2016). *Phys. Med. Biol.* **61**, 1634–1649.

Longo, R., Arfelli, F., Bonazza, D., Bottigli, U., Brombal, L., Contillo, A., Cova, M. A., Delogu, P., Di Lillo, F., Di Trapani, V., Donato, S., Dreossi, D., Fanti, V., Fedon, C., Golosio, B., Mettivier, G., Oliva, P., Pacilè, S., Sarno, A., Rigon, L., Russo, P., Taibi, A., Tonutti, M., Zanconati, F. & Tromba, G. (2019). *J. Synchrotron Rad.* **26**, 1343–1353.

Longo, R., Tonutti, M., Rigon, L., Arfelli, F., Dreossi, D., Quai, E., Zanconati, F., Castelli, E., Tromba, G. & Cova, M. A. (2014). *Philos. Trans. R. Soc. A*, **372**, 20130025.

Maldera, A., De Marco, P., Colombo, P. E., Origgi, D. & Torresin, A. (2017). *Phys. Med.* **33**, 56–67.

Mettivier, G., Fedon, C., Di Lillo, F., Longo, R., Sarno, A., Tromba, G. & Russo, P. (2016). *Phys. Med. Biol.* **61**, 569–587.

Mettivier, G., Lanconelli, N., Meo, S. L. & Russo, P. (2012*b*). *IEEE Trans. Nucl. Sci.* **59**, 2008–2019.

Mettivier, G. & Russo, P. (2011*b*). *IEEE Trans. Nucl. Sci.* **58**, 703–713.

Mettivier, G., Russo, P., Cesarelli, M., Ospizio, R., Passeggio, G., Roscilli, L., Pontoriere, G. & Rocco, R. (2011*a*). *Nucl. Instrum. Methods Phys. Res. A*, **629**, 350–356.

Mettivier, G., Russo, P., Lanconelli, N. & Meo, S. L. (2010). *IEEE Trans. Nucl. Sci.* **57**, 2510–2517.

Mettivier, G., Russo, P., Lanconelli, N. & Meo, S. L. (2012*a*). *Med. Phys.* **39**, 2805–2819.

NLM (2017). *Medline-Plus: Breast Cancer*, http://www.nlm.nih.gov/medlineplus/ency/article/000913.htm.

O'Connell, A., Conover, D. L., Zhang, Y., Seifert, P., Logan-Young, W., Lin, C. L., Sahler, L. & Ning, R. (2010). *Am. J. Roentgenol.* **195**, 496–509.

O'Connell, A., Karellas, K. & Vedantham, S. (2014). *Breast J.* **20**, 592–605.
Olivo, A., Gkoumas, S., Endrizzi, M., Hagen, C. K., Szafraniec, M. B., Diemoz, P. C., Munro, P. R. T., Ignatyev, K., Johnson, B., Horrocks, J. A., Vinnicombe, S. J., Jones, J. L. & Speller, R. D. (2013). *Med. Phys.* **40**, 090701.
Prezado, Y., Vautrin, M., Martínez-Rovira, I., Bravin, A., Estève, F., Elleaume, H., Berkvens, P. & Adam, J. F. (2011). *Med. Phys.* **38**, 1709–1717.
Rasband, W. S. (2018). *ImageJ*, https://imagej.nih.gov/ij/.
Russo, P., Coppola, T. & Mettivier, G. (2010*c*). *IEEE Trans. Nucl. Sci.* **57**, 2220–2229.
Russo, P., Lauria, A., Mettivier, G., Montesi, M. C. & Villani, N. (2010*b*). *IEEE Trans. Nucl. Sci.* **57**, 366–374.
Russo, P., Mettivier, G., Lauria, A. & Montesi, M. C. (2010*a*). *IEEE Trans. Nucl. Sci.* **57**, 160–172.
Sarno, A., Golosio, B., Russo, P., Arfelli, F., Bellazzini, R., Brez, A., Brun, F., Delogu, P., Di Lillo, F., Dreossi, D., Fedon, C., Longo, R., Mettivier, G., Oliva, P., Rigon, L., Spandre, G. & Tromba, G. (2017*a*). *IEEE Trans. Radiat. Plasma Med. Sci.* **1**, 505–510.
Sarno, A., Masi, M., Antonelli, N., Di Lillo, F., Mettivier, G., Castriconi, R. & Russo, P. (2017*b*). *IEEE Trans. Radiat. Plasma Med. Sci.* **1**, 322–328.
Sarno, A., Mettivier, G., Di Lillo, F., Cesarelli, M., Bifulco, P. & Russo, P. (2016*b*). *Med. Eng. Phys.* **38**, 1449–1457.
Sarno, A., Mettivier, G., Golosio, B., Oliva, P., Spandre, G., Di Lillo, F., Fedon, C., Longo, R. & Russo, P. (2016*a*). *Phys. Med.* **32**, 681–690.
Sarno, A., Mettivier, G. & Russo, P. (2015). *Med. Phys.* **42**, 2786–2804.
Scherer, K., Willer, K., Gromann, L., Birnbacher, L., Braig, E., Grandl, S., Sztrókay-Gaul, A., Herzen, J., Mayr, D., Hellerhoff, K. & Pfeiffer, F. (2015). *PLoS One*, **10**, e0130776.
Sechopoulos, I. (2013). *Med. Phys.* **40**, 014301.
Taba, S. T., Gureyev, T. E., Alakhras, M., Lewis, S., Lockie, D. & Brennan, P. C. (2018). *Am. J. Roentgenol.* **211**, 133–145.
Thomlinson, W., Elleaume, H., Porra, L. & Suortti, P. (2018). *Phys. Med.* **49**, 58–76.
Tomic, N., Devic, S., DeBlois, F. & Seuntjens, J. (2010). *Med. Phys.* **37**, 1083–1092.
Tomic, N., Quintero, C., Whiting, B. R., Aldelaijan, S., Bekerat, H., Liang, L. H., DeBlois, F., Seuntjens, J. & Devic, S. (2014). *Med. Phys.* **41**, 062105.
Vedantham, S., Karellas, A., Emmons, M. E., Moss, L. J., Hussain, S. & Baker, S. P. (2013). *Phys. Med. Biol.* **58**, 4099–4118.
Vedantham, S., Shi, L., Karellas, A. & O'Connell, A. (2012). *Med. Phys.* **39**, 7317–7328.